

RESEARCH ARTICLE

TBM-MSE: A Multi-Engine State Estimation Based on Inertial Enhancement for Tunnel Boring Machines in Perceptually Degraded Roadways

YU LIU¹, HONGWEI WANG^{1,2}, AND LEI TAO²¹College of Mechanical and Vehicle Engineering, Taiyuan University of Technology, Taiyuan 030024, China²Shanxi Engineering Research Center for Coal Mine Intelligent Equipment, Taiyuan University of Technology, Taiyuan 030024, China

Corresponding author: Yu Liu (liuyu0018@link.tyut.edu.cn)

This work was supported by the National Key Research and Development Program of China under Grant 2020YFB1314000.

ABSTRACT Autonomous localization and operation of tunnel boring machines in perceptually degraded roadways is essential for intelligent upgrading of tunneling. Tunneling robots are far less intelligent than anticipated owing to the darkness, dust, vibration, and geometrically degraded roadways. We presented a multi-engine state estimation method for mapping and localizing tunnel boring machines (TBM-MSE). TBM-MSE designed a novel inertial enhancement model that maintains a global consistent posture in violent vibrations. TBM-MSE constructed lever arm error compensation terms for the total station and inertial component to improve the accuracy of position constraints. Meanwhile, the multi-engine framework of the TBM-MSE adaptively adjusts the weight of the multiple sensors in dusty environments. TBM-MSE was tested on dust-free and dusty roadways. The results demonstrate that TBM-MSE was more suitable for the state estimation of tunnel boring machines than LINS and RRR-MF. TBM-MSE estimation accuracy meets actual excavation requirements. In addition, the ablation experiments further confirm the effectiveness of inertial enhancement in handling perceptually degraded environments.


INDEX TERMS Multi-engine estimation, inertial enhancement, multisensor, perceptually degraded roadways, tunnel boring machine.

I. INTRODUCTION

Compared with coal mining, tunneling mechanization development in China is stagnant. Accurate state estimation of a tunnel boring machine (TBM) is essential for achieving intelligent tunneling. Mainstream posture estimation technologies for TBM include a laser pointer, machine vision, ultra-wideband (UWB), and simultaneous localization and mapping (SLAM). Researchers constructed an automatic laser navigation system using a machine body, laser, target prism, and earth coordinate system to calculate the yaw of a TBM [1]. Some researchers established a six-degree-of-freedom (6-DOF) detection model based on machine vision and laser targets [2]. A UWB pose detection system (UPDS) for TBM was designed, which realizes the remote

posture measurement in a narrow and long enclosed roadway space [3]. The above studies should fully consider sensor posture perception accuracy. With the breakthrough of SLAM in robot pose estimation [4], [5], [6], multi-legged robots or unmanned aerial vehicles (UAVs) can deal with the underground environment without GPS. However, SLAM still faces many problems in TBM state estimation, such as the vibration noise of the oil pump motor and crawler-traveling devices during the inertial measurements; as well as the effects of roadway dust on LiDAR odometry.

The sensor errors are amplified by dust, darkness, and geometrically degraded rock walls. LiDAR odometry drifts during violent LiDAR motion; Darkness renders the camera ambiguous and tends to distort the global map; The confidence level of the inertial odometry decreases over the long-term work of the tunneling robot; Due to the excavation direction limitations of tunneling robots, loop closure

The associate editor coordinating the review of this manuscript and approving it for publication was Halil Ersin Soken .

methods are unable to deliver local optimization information for odometry. Therefore, improving the validity of sensor information in abnormal environments is an urgent problem to be solved [7]. Accurate sensor information is critical for state estimation. The primary methods for improving the performance of state estimation are two-sensor information complementation and multi-sensor fusion systems.

Researchers have used the complementary nature of sensors to improve LiDAR registration effectiveness. Motion prediction of inertial components ensures accurate convergence of LiDAR odometry [8], [9], even though the LiDAR is in motion. Fast-LIO [10] proposed a back-propagation process to compensate for the LiDAR distortion. Compensated feature primitives have rotational invariances, such as edges and surfaces [11]. Using curvature labels to extract these features can increase the validity of point cloud registration [12]. Based on the complementarity of sensor information, researchers have explored multisensor fusion models to integrate two or even more types of perception information. The fusion systems involving LiDAR and inertial components can be divided into loosely coupled and tightly coupled methods. Loosely coupled systems ignore high-order errors and linearization site selection during the independent state estimation of each sensor, which reduces the estimation accuracy. On the other hand, the feature fusion that fully considers the inherent relationship between sensors is referred to as tightly coupled [13], [14], [15]. The iterated extended Kalman filter (IEKF) methods [16], [17], [18] are commonly used for tightly coupled that correct linearization errors. The tightly coupled INS integration has achieved significant advancements in eliminating a tremendous amount of redundant computation in the prediction process [19], correcting sensitivity to measurement errors [20], and improving fusion performance [21].

To reduce the risk of loosely coupled or tightly coupled single-engine estimation, multi-sensor distribution fusion has increasingly drawn attention from researchers. The mainstream technical route of multi-sensor data fusion combines local decentralized fusion and optimal global fusion to improve the accuracy and reliability of integrated navigation systems [22], [23]. Recently, LiDAR has gradually become a primary sensor of posture perception. Multi-sensor data fusion combined with Lidar odometry has also become a popular research direction. Super Odometry [24] was the first to propose an estimation framework that considers both loosely coupled and tightly coupled methods. The inertial navigation estimation of Super Odometry was loosely coupled, while vision-inertial and LiDAR-inertial odometry components were tightly coupled methods. RRR-MF [25] adhered to the concept of multi-engine fusion. An error state Kalman filter (ESKF) fused the inertial component and total station data; the filtered result was treated as a factor and added to the factor graph along with the LiDAR odometry factor. The LiDAR-centric SLAM framework is a reliable localization method for autonomous robots in GNSS-denied

environments [26]. However, dust roadway challenges the accuracy of LiDAR measurements. Inertial navigation estimation constitutes the primary means for removing LiDAR distortions. Therefore, inertial estimation needs to be robust and may even make a significant contribution to the results.

However, inertial components are typically regarded as auxiliary sensors with low-weight factors when information complementarity or multi-sensor fusion systems are utilized under complex conditions. Researchers have investigated the effects of complexity and instability of external vibration on inertial navigation estimation, enhanced the reliability of inertial measurement, and improved the weight of the fusion system. Currently, the primary methods of enhancing the effectiveness of inertial measurement include discrete wavelet threshold filtering (DWTf) and empirical mode decomposition (EMD). The researchers proposed the Wavelet Packet Transform-Chaos Particle Swarm Optimization-Back Propagation Neural Network (WPT-CLSPSO-BP) method to decompose the signal containing vibration noise and fully reconstruct the valuable information [27]. To remove the jitter and interference caused by the inertial measurement unit (IMU) at the speed over group and course over group, the researchers implemented the EMD noise reduction algorithm for trajectory reconstruction [28]. DFA-EMD combined detrended fluctuation analysis (DFA) and empirical mode decomposition (EMD) to reduce fiber optic gyroscope (FOG) random noise and drift [29]. A neural network (NN) prediction model and wavelet packet transform (WPT) technology were simultaneously incorporated into the EMD method to improve the denoising ability [30]. Although the aforementioned techniques effectively reduced drift errors, the vibration noise generated by oil pump motors and crawler-traveling devices posed a challenge to these methods. Therefore, this paper proposes a novel multi-engine estimation method with an inertial enhancement model to improve posture perception accuracy and attain globally consistent state estimation.

Motivated by the aforementioned discussion, this paper presents the development and implementation of an inertial enhancement-centric multi-engine estimation, which serves as a critical enabler for TBM localization in perceptually degraded environments. An overview of our framework is shown in Figure. 1. The primary contributions of TBM-MSE are as follows:

1. TBM-MSE creates an inertial enhancement model to reduce vibration and non-exchangeable errors from the oil pump motor and crawler-traveling devices.
2. TBM-MSE designs an INS/total station coupled filter with lever arm error compensation terms to enhance the independence and accuracy of the position constraint.
3. TBM-MSE proposes multi-engine estimation to ensure the validity of LiDAR registrations and the global consistency of the estimated state in perceptually degraded roadways.

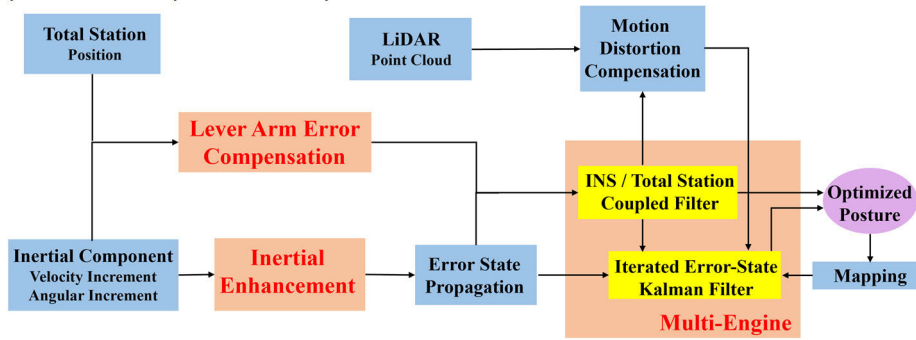


FIGURE 1. An overview of the TBM-MSE.

For the purpose of enhancing the validity of state perception, there is a coherent relationship between these three contributions, forming a more robust and accurate TBM state estimation system. The inertial enhancement model primarily enhances the precision of attitude estimation (roll, pitch, yaw), and the error compensation of the lever arm focuses on the correction of position estimation (x, y, z). Together, they form an INS/total station coupled filter to deliver an improved 6-DOF state estimation of the TBM. Environmental characteristics markedly influence LiDAR, but LiDAR odometry can rectify the outcomes produced by the INS/total station coupled filter in favorable working conditions. Additionally, the multi-engine estimation can maximize the advantage of LiDAR without cumulative error, further enhancing the entire system’s accuracy and reliability.

The remaining paper is organized as follows: We present the details of each key component in Section. II. The experimental results are presented in Section. III. We design the ablation experiment in Section. IV. The conclusions in Section. V.

II. METHODOLOGY

A. INERTIAL ENHANCEMENT MODEL

TBM-MSE minimizes nonlinear and nonsmoothed vibration noise produced by oil pump motors and crawler traveling devices by an inertial enhancement that consists of inertial measurement pre-processing and inertial navigation system mechanization optimization.

Pre-processing techniques of the TBM-MSE include oil pump noise compensation and internal parameters recalibration. The time-domain and frequency-domain analyses of the TBM vibration characteristics reveal that static measurements are destroyed by oil pump noise, such as the fluctuations of X-axis specific force and X-axis angular velocity in Figure. 2.

TBM-MSE adopts a novel empirical mode decomposition to rapidly sift and reconstruct the intrinsic mode functions (IMFs) [31]. TBM-MSE converts raw measurements $x(t)$ into IMF components and trend terms. Autonomously discriminates the boundary parameters M of IMFs by the Euclidean

distance. The $\hat{x}(t)$ indicates the initial reconstruction result.

$$x(t) = \sum_{i=1}^n IMF_i + r_n(t) = \sum_{i=1}^n S_i(t) + r_n(t) \quad (1)$$

$$\hat{Z}_k(t) = \sum_{i=k}^n S_i(t) + r_n(t) \quad (2)$$

$$M = \arg \min_{1 \leq k \leq n-1} \left[\frac{1}{N} \sum_{i=1}^N [Z_{k+1}^\wedge(t_i) - \hat{Z}_k(t_i)]^2 \right] \quad (3)$$

$$\hat{x}(t) = \sum_{i=M}^n S_i(t) + r_n(t) \quad (4)$$

where N is the number of sampling points and t_i is the sampling moment. Based on the TBM vibration noise characterization, TBM-MSE uses a soft threshold to optimize the signal.

$$\hat{S}_i(z_j^i) = \begin{cases} S_i(z_j^i) \frac{|S_i(r_j^i)| - T_i}{|S_i(r_j^i)|}, & |S_i(r_j^i)| > T_i \\ 0, & |S_i(r_j^i)| \leq T_i \end{cases} \quad (5)$$

$$T_i = \sqrt{\hat{\sigma}_i^2 2Ln(N)} \quad (6)$$

$$\hat{\sigma}_i = \frac{\text{median}(|S_i(t)|)}{0.6745} \quad (7)$$

where $z_j^i = [z_j^i, z_{j+1}^i]$ is the j th zero-crossings interval in the i th IMF, r_j^i is the single extremum in $z_j^i = [z_j^i, z_{j+1}^i]$. The σ indicates the noise variance. After suppressing the vibration noise of the oil pump, TBM-MSE re-calibrates the Gaussian white noise b and random wandering noise w [32].

Assuming that the inertial system (i) coincides with the carrier coordinate system (b), $T_i^b = I$; T_{TS}^i represents the relative transformation from total station prism (TS) to the inertial component (i), $T_{TS}^i = T_{TS}^b$; T_L^i indicates external parameters of LiDAR and the inertial component (i), $T_L^i = T_L^b$. This paper adopts the North-East-Down (NED) coordinate system (n).

The inertial navigation system mechanizations optimization contains two components: error compensation of crawler

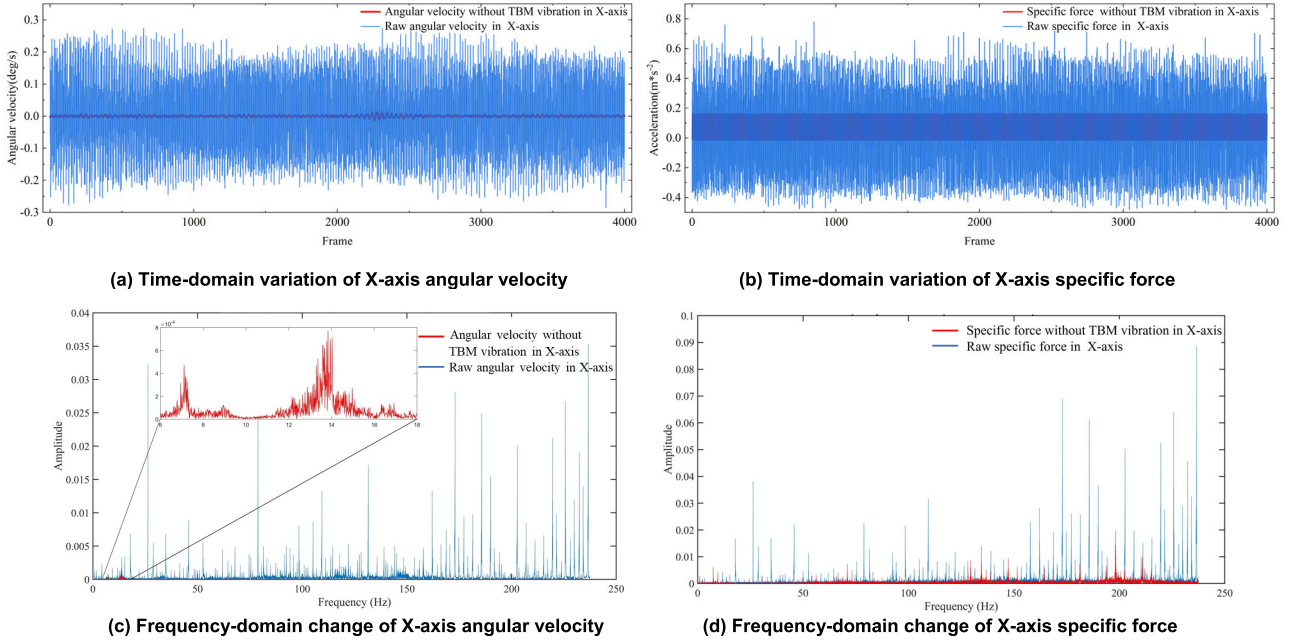


FIGURE 2. Fluctuation in INS mechanization after the oil pump working.

traveling devices and static attitude correction. The state differential formula can be solved by the Peano-Baker approximation, which ignores the nonexchangeable error of the actual attitude change. Increasing the output frequency of dead reckoning can effectively avoid the cone error impact. After experimental testing and evaluation, the output frequency was raised to 475Hz.

The equivalent rotation vector ϕ_k is created by the double sampling of the angular velocity vector $\omega_{ib}(t)$ [33], $\Delta\theta_k$ indicates the angular increment in $[t_k, t_{k+1}]$. Updating the direction cosine matrix $C_{b(k)}^n$ in a discrete-time system, TBM-MSE ignores the transformation of navigation coordinate systems during the movement. $\phi_k \times$ represents the skew-symmetric matrix of ϕ_k .

$$\begin{aligned} \phi_k &= \int_{t_{k-1}}^{t_k} \omega_{ib}(t) dt + \frac{1}{12} \int_{t_{k-2}}^{t_{k-1}} \omega_{ib}(t) dt \\ &\quad \times \int_{t_{k-1}}^{t_k} \omega_{ib}(t) dt \\ &= \Delta\theta_k + \frac{1}{12} \Delta\theta_{k-1} \times \Delta\theta_k \end{aligned} \quad (8)$$

$$C_{b(k)}^n \approx C_{b(k-1)}^n C_{b(k)}^{b(k-1)} \quad (9)$$

$$C_{b(k)}^{b(k-1)} = I + \frac{\sin \phi_k}{\phi_k} (\phi_k \times) + \frac{1 - \cos \phi_k}{\phi_k^2} (\phi_k \times)^2 \quad (10)$$

The influence of the paddle effect is reduced by double sampling both angular velocity vector $\omega_{ib}(t)$ and specific force vector $f(t)$, Δv_k indicates the velocity increment in $[t_k, t_{k+1}]$. The position p_k^n update depends on the velocity v_k^n .

$$v_k^n \approx v_{k-1}^n + C_{b(k-1)}^{n(k-1)} \left(\int_{t_{k-1}}^{t_k} f(t) dt \right)$$

$$\begin{aligned} &+ \frac{1}{2} \int_{t_{k-1}}^{t_k} \omega_{ib}(t) dt \times \int_{t_{k-1}}^{t_k} f(t) dt \\ &+ \frac{1}{12} \left(\int_{t_{k-2}}^{t_{k-1}} \omega_{ib}(t) dt \times \int_{t_{k-1}}^{t_k} f(t) dt \right. \\ &\quad \left. + \int_{t_{k-2}}^{t_{k-1}} f(t) dt \times \int_{t_{k-1}}^{t_k} \omega_{ib}(t) dt \right) \\ &\approx v_{k-1}^n + C_{b(k-1)}^{n(k-1)} \left\{ \Delta v_k + \left(\frac{1}{2} \Delta\theta_k \right) \times (\Delta v_k) \right. \\ &\quad \left. + \frac{1}{12} [(\Delta\theta_{k-1}) \times (\Delta v_k) + (\Delta v_{k-1}) \times (\Delta\theta_k)] \right\} \end{aligned} \quad (11)$$

$$p_k^n = p_{k-1}^n + \frac{v_k^n + v_{k-1}^n}{2} (t_k - t_{k-1}) \quad (12)$$

The motion characteristics of TBM increase the sensitivity of gyroscope measurements. Attitude update methods that rely on gyroscope measurements are unreliable. According to the TBM kinematics and sensors error characteristics, TBM-MSE modifies attitude by static acceleration value. We establish the attitude accelerometer correction term $\Delta q'_{acc}$ based on the orientation filter [34]. In this paper, the parameters of adaptive gain α in $\Delta q'_{acc}$ are optimized to match the actual accelerometer output of TBM. The $\alpha = L(e_m)$ adaptively adjusts state estimation weights of the accelerometer and gyroscope for different motion states of TBM.

$$\alpha = L(e_m) = 0.991 / (1 + e^{\frac{2500e_m - 370}{40}}) \quad (13)$$

$$e_m = \frac{\|f + [0, 0, g_p]^T\| - g_p}{g_p} \quad (14)$$

where $\| \cdot \|$ denotes the norm of the acceleration vector, $g_p = 9.81 \text{ m/s}^2$. When f changes dramatically, α is close to zero and $\Delta q'_{acc}$ approaches $[1 \ 0 \ 0 \ 0]^T$; otherwise, α is almost equal

to 1, $\Delta q'_{acc}$ corrects attitude $q_{b(k)}^{b(k-1)}$. The gain $\alpha = L(e_m)$ of TBM-MSE increases the smoothness of the output.

$$\text{Correction } q_{b(k)}^{b(k-1)} = q_{b(k)}^{b(k-1)} \circ \Delta q'_{acc} \quad (15)$$

B. INS/TOTAL STATION COUPLED FILTER

Due to the complexity of roadway environments, this paper proposes a multi-engine coupling state estimator. TBM-MSE is composed of loosely coupled filters and tightly coupled filters. TBM-MSE considers the inertial error model and simplifies the observations, and compensates for lever arm errors between the prism and inertial component.

1) STATE DEFINITIONS

Based on operations “ \boxplus ” and “ \boxminus ” defined in [35], the relationships between the actual state X_{true}^n and error state δX^n are as follows:

$$\begin{cases} \overline{p}^n = p_{true}^n + \delta p^n \\ \overline{v}^n = v_{true}^n + \delta v^n \\ \overline{C}_b^n = C_{b,true}^n \boxplus \exp(\phi) \\ \overline{w}_{ib}^b = w_{ib,true}^b + \delta w_{ib}^b \\ \overline{f}^b = f_{true}^b + \delta f^b \end{cases} \quad \delta X^n = [(\delta p^n)^T \quad (\delta v^n)^T \quad \phi^T \quad (b_g)^T \quad (b_a)^T]^T, \quad (16)$$

where \overline{p}^n , \overline{v}^n , and \overline{C}_b^n are outputs of inertial enhancement model; w_{ib}^b and f^b are the actual measurements. The sensor error model includes bias b and Gaussian white noise w :

$$\delta w_{ib}^b = b_g + w_g, \quad \delta f^b = b_a + w_a \quad (17)$$

where w_g and w_a are Gaussian white noise of the gyroscope and accelerometer. To overcome the effect of the roadway on the random bias error, accelerometer bias b_a and gyroscope bias b_g are considered first-order Markov processes in the time interval T :

$$\dot{b}_g = \frac{1}{T} b_g + w_{gb}, \quad \dot{b}_a = \frac{1}{T} b_a + w_{ab} \quad (18)$$

where w_{gb} and w_{ab} denote the driven white noise of the gyroscope and accelerometer, respectively.

2) ERROR STATE EQUATIONS

The differential formula of the error state δX is

$$\dot{\delta X} = F_k \delta X + G_k W \quad (19)$$

$$F_k = \begin{pmatrix} 0 & I_{3 \times 3} & 0 & 0 & 0 \\ 0 & 0 & (C_b^n f_{true}^b) \times & 0 & C_b^n \\ 0 & 0 & -(\omega_{in}^n \times) & -C_b^n & 0 \\ 0 & 0 & 0 & \frac{1}{T} I_{3 \times 3} & 0 \\ 0 & 0 & 0 & 0 & \frac{1}{T} I_{3 \times 3} \end{pmatrix},$$

$$G_k = \begin{pmatrix} 0 & 0 & 0 & 0 \\ 0 & C_b^n & 0 & 0 \\ -C_b^n & 0 & 0 & 0 \\ 0 & 0 & I_{3 \times 3} & 0 \\ 0 & 0 & 0 & I_{3 \times 3} \end{pmatrix},$$

$$W = [w_g \quad w_a \quad w_{gb} \quad w_{ab}]^T \quad (20)$$

where

$$\omega_{in}^n = \left[\omega_e \cos \varphi + \frac{v_E}{R_N + h} \frac{-v_N}{R_M + h} \quad -\omega_e \sin \varphi - \frac{v_E \tan \varphi}{R_N + h} \right]^T,$$

ω_{in}^n represents the projection of the angular velocity vector under the navigation system, R_M and R_N are curvature radius of the meridian and prime vertical, angular velocity of earth rotation $w_e = 7.2921 \times 10^{-5} \text{ rad/s}$.

3) PROPAGATION EQUATIONS

The discrete propagation model and the covariance matrix of error state are as follows, Q_w denotes system noise covariance that is computed off-line during recalibration:

$$\begin{cases} \delta \hat{X}_k = (I + F_k \Delta t) \delta \hat{X}_{k-1} \\ \hat{P}_k = (I + F_k \Delta t) \hat{P}_{k-1} (I + F_k \Delta t)^T + (G_k \Delta t) Q_w (G_k \Delta t)^T \end{cases} \quad (21)$$

4) TOTAL STATION MEASUREMENTS

Only independent position errors are considered observations when the TBM-MSE enhances posture constraints in a GPS-denied roadway. Meanwhile, TBM-MSE proposes a compensation model for lever arm error of the prism and inertial component, which reduces the Z-axis drift of the position estimation. The z is position errors between measurement and observation,

$$z \approx \delta p^n + (C_b^n I_{TS}^{INS} \times) \hat{\phi} + n_{TS} \quad (22)$$

where δp^n and $\hat{\phi}$ are estimation errors, I_{TS}^{INS} represents the three-dimensional vector pointing from inertial component to prism, $I_{TS}^{INS} = [0.0918m \quad -0.8221m \quad -0.384m]^T$, as shown in Figure. 3; The measurement error of the total station n_{TS} is modeled as a white noise sequence, $n_{TS} \in N(0, Q_{TS})$. Creating an observation matrix H_{TS} for position errors from total station data, $H_{TS} = [I_3 \quad 0_3 \quad (C_b^n I_{TS}^{INS} \times) \quad 0_3 \quad 0_3 \quad 0_3 \quad 0_3]$.

5) UPDATE

$$K_k = \hat{P}_k H_{TS,k}^T (H_{TS,k} \hat{P}_k H_{TS,k}^T + Q_{TS})^{-1} \quad (23)$$

$$\delta \hat{X}_k = \delta \hat{X}_k + K_k (z_k - H_{TS,k} \delta \hat{X}_k) \quad (24)$$

$$\hat{P}_k = (I - K_k H_k) \hat{P}_k \quad (25)$$

The INS/total station coupled filter adjusts the weight of redundant errors between predictions and observations by K_k . $ins X_k^n$ indicates the output of inertial estimation and $e X_k^n$ is the output of INS/total station coupled filter in the navigation coordinate system:

$$e X_k^n = ins X_k^n \boxplus \delta \hat{X}_k \quad (26)$$

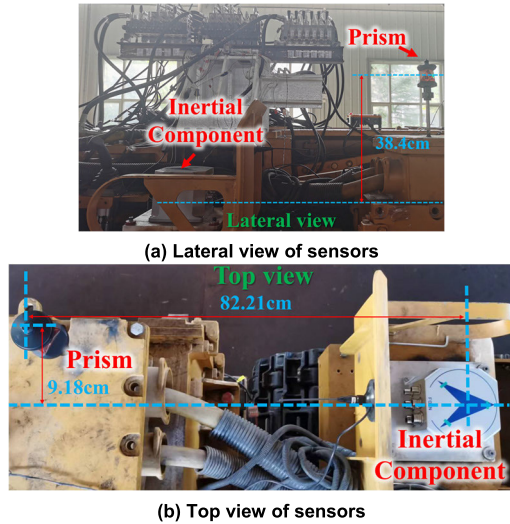


FIGURE 3. The relative position of the total station prism and inertial component on the TBM.



FIGURE 4. Hardware. The modified drilling arm was attached to the right side of the TBM. All sensors were mounted in the middle of the TBM. The LiDAR was located above the inertial component.

C. ITERATED ERROR-STATE KALMAN FILTER

1) PROPAGATION EQUATIONS

The propagation equations of iterated Kalman filter are the same as INS/total station coupled filter.

2) LIDAR MOTION DISTORTION COMPENSATION

TBM-MSE inputs ${}^e X_k^n$ as an initial value into the iterated error-state filter. The oil pump motor and the crawler traveling devices cause TBM to shake violently, which exacerbates the LiDAR nonuniform motion. TBM-MSE compensates for movement distortion by ${}^e X_k^n$. The t_i is adjacent to the timestamps τ_j and τ_{j+1} in ${}^e X_k^n$. These corresponding postures $T_{b,j}^{n(k)}$ and $T_{b,j+1}^{n(k)}$ ($T = \{C, p\}$) are used to estimate the pose $T_{b,i}^{n(k)}$ at t_i [36].

$$T_{b,i}^{n(k)} = \frac{t_i - \tau_j}{\tau_{j+1} - \tau_j} T_{b,j+1}^{n(k)} + \frac{\tau_{j+1} - t_i}{\tau_{j+1} - \tau_j} T_{b,j}^{n(k)} \quad (27)$$

The $T_{b, \text{end}}^{n(k)}$ is the end posture of the k_{th} LiDAR scan. Calculating T_i^{end} is the essence of eliminating motion distortion. Then the point ${}^k p_i$ is projected into the NED, represented by ${}^k p_i^n$.

$$T_{b,i}^{n(k)} = T_{b, \text{end}}^{n(k)} (T_i^{\text{end}}) \quad (28)$$

$${}^k p_i^n = (T_{b, \text{end}}^{n(k)} (T_i^{\text{end}})) T_L^b ({}^k p_i) \quad (29)$$

TBM-MSE extract line and surface features by magnitude relationship between the eigenvalues. Assume $x_j (j = 1, 2, \dots, n)$ are the nearest point clouds to p_i , S represents covariance matrix,

$$S_{3 \times 3} \approx YY^T \quad (30)$$

where $Y = [y_1 \dots y_n]$, $y_j = x_j - p_i$. The λ indicates the eigenvalue of S . The u is the corresponding eigenvector of S . If $\lambda_1 \geq \lambda_2 \geq \lambda_3$, $\frac{|\lambda_1 - \lambda_2|}{|\lambda_2 - \lambda_3|} \leq \gamma$, p_i belongs to F_{plane} , λ_3 and u_3

are retained; when $\frac{|\lambda_1 - \lambda_2|}{|\lambda_2 - \lambda_3|} \geq \Gamma$, p_i belongs to F_{edge} , λ_1 and u_1 are retained. The F_{edge} and F_{plane} are used to construct the local map ${}^{\text{map}} p_i$. According to the experimental results, $\gamma = 0.37$, $\Gamma = 2.1$.

3) LIDAR MEASUREMENTS

TBM-MSE fuses LiDAR observation with the error state $(\delta X_k, P_k)$. To obtain dense mapping results and efficient dynamic data updates, TBM-MSE maintains a map by ikd-Tree [17]. The ${}^k p_i^n$ can search for corresponding feature primitives in the local map ${}^{\text{map}} p_i$. TBM-MSE takes eigenvectors to construct distance residuals:

$$z(X_k^n, 0) \begin{cases} \frac{|{}^{\text{map}} u_{i,1} \times (({}^{\text{map}} p_i) - ({}^k p_i^n))|}{|{}^{\text{map}} u_{i,1}|} & {}^k p_i^n \in F_{\text{edge}} \\ |{}^{\text{map}} u_{i,3} \cdot (({}^{\text{map}} p_i) - ({}^k p_i^n))| & {}^k p_i^n \in F_{\text{plane}} \end{cases} \quad (31)$$

The actual point cloud ${}^{g,t,k} p_i^n$ contains LiDAR measurement noise n_L . The corresponding residuals are represented as $z(X_k^n, n_L)$. The following expression is obtained by approximating residual $z(X_k^n, n_L)$ with first-order approximation at ${}^r X_{op,k}^n$.

$${}^{g,t,k} p_i^n = {}^k p_i^n - n_L \quad (32)$$

$$z(X_k^n, n_L) \approx z({}^r X_{op,k}^n, 0) + {}^r M_k \cdot (X_k^n \boxminus {}^r X_{op,k}^n) + u_L \quad (33)$$

$${}^r M_k = \frac{\partial z(X_k^n, n_L)}{\partial X_k^n} \Big|_{{}^r X_{op,k}^n, 0} \quad (34)$$

$${}^r \delta X_k = X_k^n \boxminus {}^r X_{op,k}^n \quad (35)$$

where r denotes the number of iterations, $u_L \in N(0, Q_L)$ comes from LiDAR measurement noise n_L . ${}^r X_{op,k}^n$ is the optimal state in iteration, its initial state is ${}^e X_k^n$.

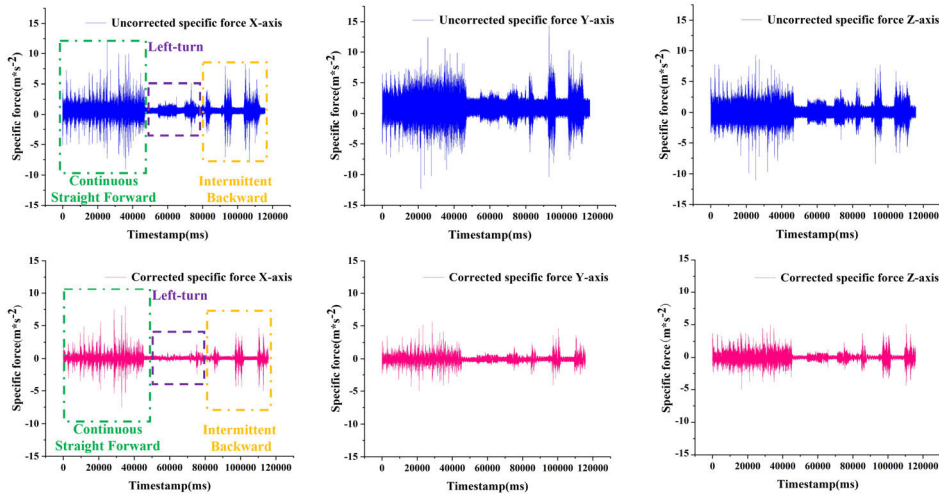


FIGURE 5. Time domain variation curve of specific force after inertial enhancement. In the three motion states of the TBM, the fluctuation of the specific force is significantly reduced and the bias is also corrected.

4) RESIDUAL COMPUTATION

Based on the initial state of the INS/total station coupled filter and observation residuals, TBM-MSE treats the error state update as an optimization problem. The following formula is constructed via Mahalanobis distance:

$$\min_{\delta x} (\|{}^r \delta X_k\|_{({}^r P_k)^{-1}}^2 + \|z({}^r X_{op,k}^n, 0) + M_k {}^r \delta X_k\|_{(Q_L)^{-1}}^2) \quad (36)$$

5) ITERATED UPDATE

Formula (36) can be solved by the following formulas,

$${}^r D_k = \frac{\partial z({}^r X_{op,k}^n, n_L)}{\partial {}^k p_i^n} \cdot \frac{\partial {}^k p_i^n}{\partial \delta X_k} \quad (37)$$

$${}^r J_k = \frac{\partial z({}^r X_{op,k}^n, n_L)}{\partial {}^k p_i^n} \cdot \frac{\partial {}^k p_i^n}{\partial n_L} \quad (38)$$

$${}^r K_k = {}^r P_k {}^r D_k^T ({}^r D_k {}^r P_k {}^r D_k^T + {}^r J_k Q_L {}^r J_k^T)^{-1} \quad (39)$$

$${}^{r+1} \delta X_k = {}^r \delta X_k \boxplus {}^r K_k ({}^r D_k ({}^r \delta X_k) - z({}^r X_{op,k}^n, 0)) \quad (40)$$

$${}^{r+1} P_k = (I - {}^r K_k {}^r D_k) {}^r P_k (I - {}^r K_k {}^r D_k) + {}^r K_k Q_L {}^r K_k^T \quad (41)$$

where the initial state of ${}^r P_k$ is \hat{P}_k . If formula (36) converges, the error state ${}^r \delta X_k$ and the optimal estimation state ${}^{r+1} X_{op,k}^n$ stop updating.

$${}^{r+1} X_{op,k}^n = {}^r X_{op,k}^n \boxplus {}^{r+1} \delta X_k \quad (42)$$

III. EXPERIMENT RESULTS

A. SYSTEM HARDWARE

The system hardware included a LiDAR (Velodyne), an inertial component (FOSN II), and a total station (TS60), as shown in Figure. 4. TBM-MSE was deployed on a tunnel boring machine (EBZ160M-2).

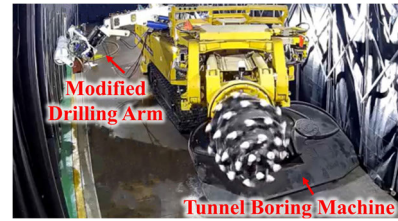


FIGURE 6. The working environment of the tunnel boring machine. TBM-MSE was deployed on a modified TBM and tested in a simulated roadway, 25m × 5m × 4 m.

TABLE 1. Effect of vibration on initial attitude.

initial attitude angle	roll	pitch	yaw
without vibration noise	0.01°	0.31°	177.67°
with vibration noise	0.01°	0.30°	177.29°

TABLE 2. Initial attitude after inertial enhancement.

initial attitude angle	roll	pitch	yaw
vibration suppression	0.01°	0.31°	177.60°

B. THE RESULT OF INERTIAL ENHANCEMENT

Static initialization results and dynamic measurement stability demonstrated the necessity of inertial enhancement. The vibration noise of the oil pump interferes with the accuracy of the static initialization, as shown in Table 1, the yaw error was about 0.4°. After inertial enhancement, the error of the yaw initialization result was reduced by 81.57 %, as shown in Table 2.

TBM-MSE recalibrates internal parameters. The results were, as shown in the equation at the bottom of the next page.

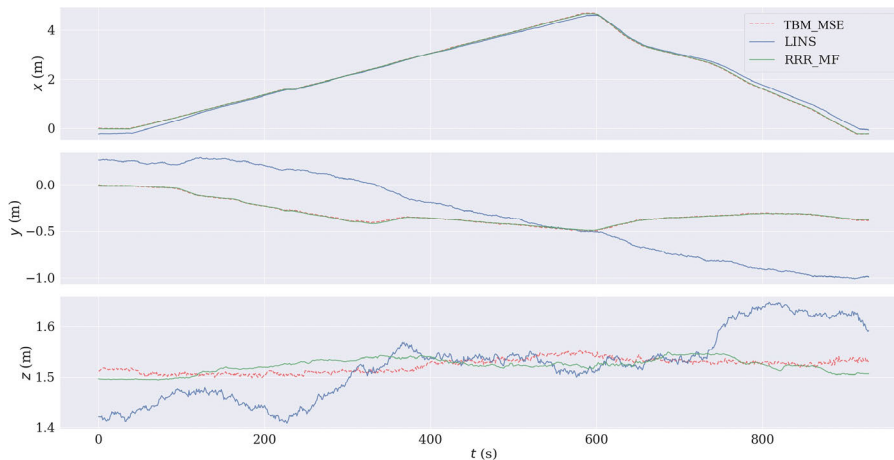


FIGURE 7. The position estimation results of TBM-MSE, LINS, and RRR-MF in a dust-free roadway.

With inertial enhancement, inertial measurements can resist external vibrations during the three motion states: continuous straight forward, turning, and intermittent backward. Taking specific force as an example, Figure. 5 displayed the change after inertial enhancement. Combining the static initialization results and dynamic inertial measurements, the inertial enhancement model improves the robustness of inertial estimation.

C. STATE ESTIMATION IN DUSTFREE ROADWAYS

Based on our previous work [25], TBM-MSE only uses independent position errors to solve the Z-axis drift problem. The TBM is set to move forward 4.70 m and then return to the starting position, as shown in Figure. 6. TBM-MSE was compared with LINS [16] and RRR-MF [25] in terms of trajectory estimation, as shown in Figure. 7.

By analyzing the trajectory curves of the three methods, we can accurately evaluate the posture initialization and real-time position estimation accuracy. The actual initial position in the carrier coordinate system was (0m, 0m, 1.5m). The trajectories of the TBM-MSE and RRR-MF differed by a few millimeters. LINS was the most significant Z-axis drift, with an error range of ±0.10 m. The Z-axis position estimation errors of the TBM-MSE and RRR-MF were nearly identical, which were 3/20 of LINS. At the same time, the average error in the Y-axis for LINS exceeded 0.25 m. In the dust-free roadway, the localization capabilities of TBM-MSE and RRR-MF were equivalent. RRR-MF is an optimization-based algorithm that relies on the accuracy of LiDAR odometry to ensure consistent global estimation.

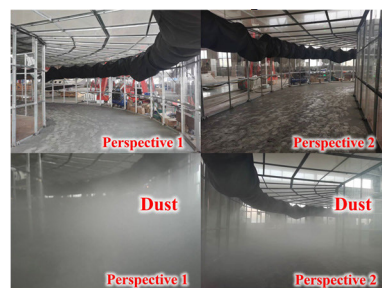


FIGURE 8. The dust removal system. To simulate the real working environment of TBM, the simulated roadway is filled with dust, and the concentration of dust exceeds 200mg/m³.

D. STATE ESTIMATION IN DUST ROADWAYS

The dust weakens the accuracy of LiDAR odometry. We proposed a multi-engine coupling framework to lessen reliance on LiDAR odometry. We established a dust removal system, as shown in Figure. 8. TBM-MSE was compared with LINS and RRR-MF in terms of mapping, position estimation, and attitude estimation in dusty, as shown in Figure. 9, Figure 10, and Figure 11.

The significant estimation drift of RRR-MF led to mapping failure in the dust. The RRR-MF has no comparative value because of the significant estimation errors. The mapping results of TBM-MSE outperform LINS in terms of map accuracy and density. There were significant mistakes in LINS mapping, which marked objects at the same height in reality with different colors, as shown in Fig. 9(c). The LINS mapping only had 19 sub-maps and TBM-MSE’s map consists of 940 submaps.

$$[b_g \quad b_a \quad w_g \quad w_a] \approx \begin{bmatrix} 9.2319 \times 10^{-5} & 1.4079 \times 10^{-2} & 3.8473 \times 10^{-7} & 1.0486 \times 10^{-4} \\ 4.1794 \times 10^{-6} & 6.1506 \times 10^{-1} & 5.4798 \times 10^{-8} & 5.8065 \times 10^{-3} \\ 3.8778 \times 10^{-5} & 7.3013 \times 10^{-3} & 1.2390 \times 10^{-7} & 3.8272 \times 10^{-5} \end{bmatrix}$$

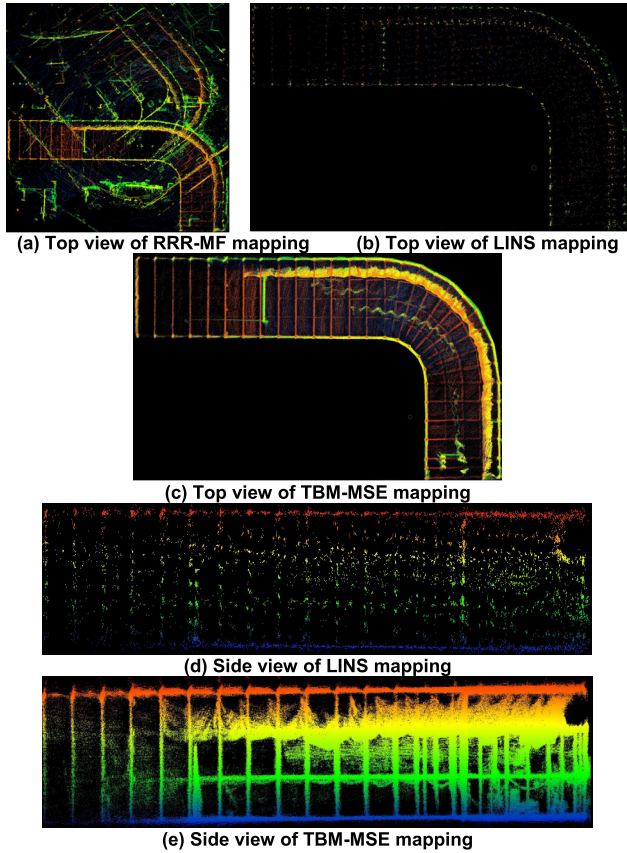


FIGURE 9. The mapping results of RRR-MF, LINS, and TBM-MSE.

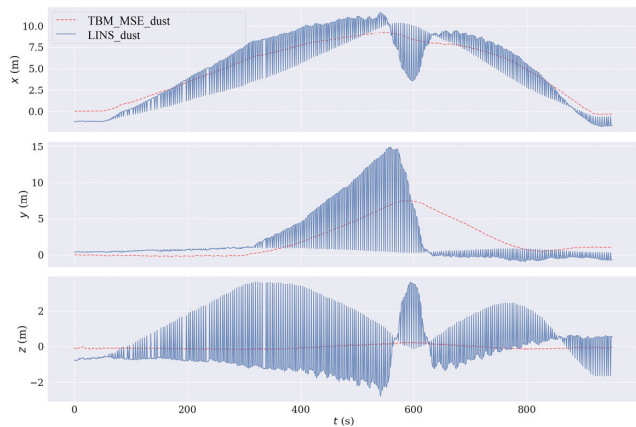


FIGURE 10. Position estimation of TBM-MSE and LINS. LINS drifts more than 2m in the three axes.

The average drift of the LINS Z-axis trajectory increased to 3.263m, indicating that the dust further amplified the state estimation error. However, there was no apparent drift in the TBM-MSE mapping or the position estimation. Compared with the TBM-MSE, the attitude angle of LINS fluctuated more than 50°, as shown in Figure. 11. The bottom of the dust roadway was generally flat, so the roll and pitch estimated by LINS are unrealistic.

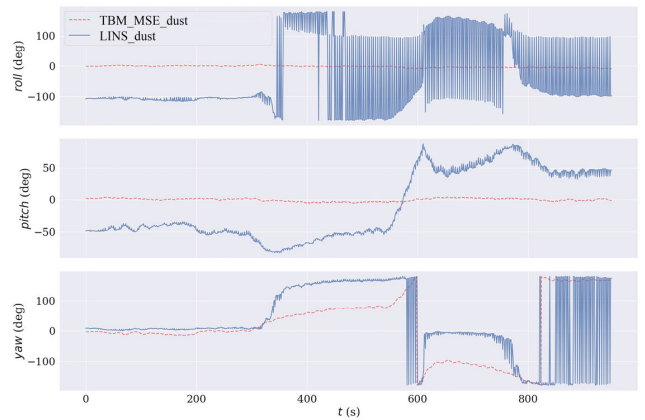


FIGURE 11. Attitude angle estimation of TBM-MSE and LINS in the dust.

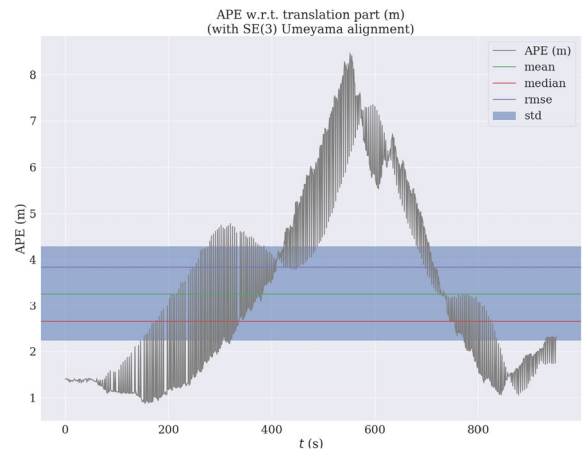


FIGURE 12. APE between TBM-MSE and LINS.

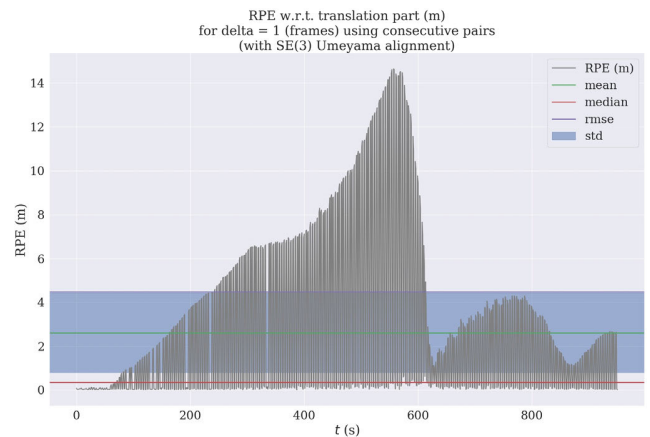


FIGURE 13. RPE between TBM-MSE and LINS.

This paper quantifies the difference in localization between TBM-MSE and LINS in dust by absolute pose error (APE) and relative pose error (RPE), using the result of TBM-MSE as a reference, as shown in Figure. 12 and Figure. 13. The error indicators for LINS were illustrated in Table 3 and Table 4.

TABLE 3. APE indicators of TBM-MSE and LINS.

maximum	minimum	mean	median	root mean squared error	standard deviation
8.46m	0.878m	3.26m	2.65m	3.84	2.038

TABLE 4. RPE indicators of TBM-MSE and LINS.

maximum	minimum	mean	median	root mean squared error	standard deviation
14.63m	0.005m	2.62m	0.34m	4.49	3.651

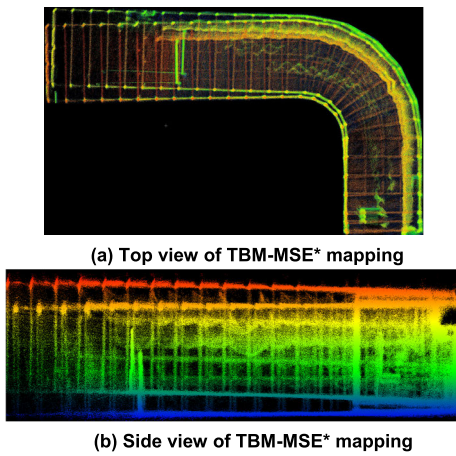


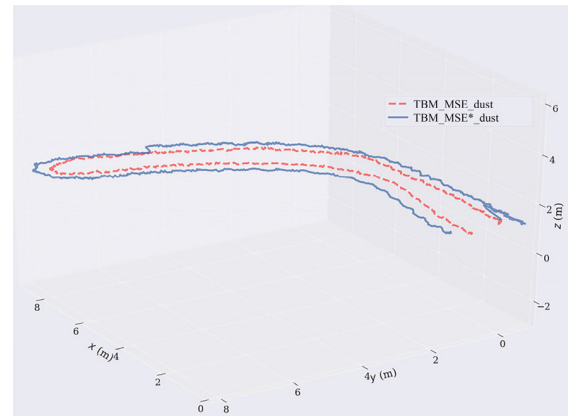
FIGURE 14. The mapping of TBM-MSE*. TBM-MSE* produced ghosting in the mapping after a left turn.

Dust caused huge posture estimation errors in RRR-MF, while LINS was also impacted by dust, and its estimation results demonstrated more severe drift than the dust-free roadway. In conclusion, TBM-MSE is the most effective framework for real-time TBM state estimation in perceptually degraded roadways.

IV. ABLATION EXPERIMENT

The essence of the TBM-MSE is to make the inertial estimation more robust under challenging environments. TBM-MSE without an inertial enhancement model was distinguished by * to investigate the effect of inertial measurement pre-processing and inertial navigation system mechanization optimization in initialization, mapping, and localization. The results are shown in Figure. 14 and 15.

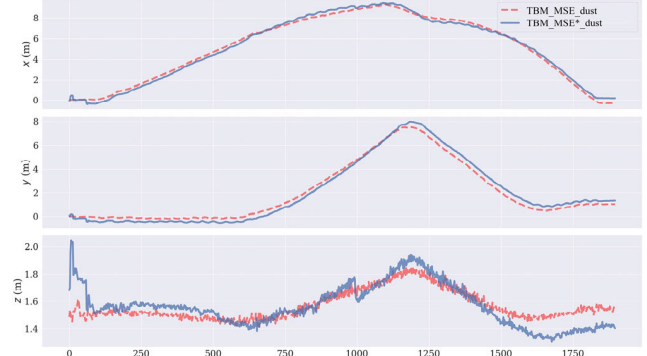
The position estimation error of the TBM-MSE* led to ghosting in mapping, as shown in Figure. 14(a) and Figure. 15(a). TBM-MSE* had huge initialization errors. At the beginning of state estimation, there were significant fluctuations in the Z-axis position, roll, and pitch. TBM-MSE* was affected by the TBM vibration, so the pitch and



(a) The global trajectory estimation of TBM-MSE and TBM-MSE*



(b) Trajectory estimation of TBM-MSE and TBM-MSE* in three directions



(c) The attitude angle estimation of TBM-MSE and TBM-MSE*

FIGURE 15. The posture estimation of TBM-MSE* and TBM-MSE.

roll amplitude changes were more dramatic. In summary, the localization of TBM benefits from the inertial enhancement model.

V. CONCLUSION

This paper introduces the TBM-MSE, a novel multi-engine estimation method that focuses on inertial enhancement for autonomous localization in coal mine roadways, specifically designed for applications on TBM. A robust inertial enhancement model has been developed and validated, improving the accuracy of posture perception. Ablation experiments have demonstrated that this model can suppress vibration noise caused by the oil pump motor and crawler traveling devices, reduce attitude initialization errors, and enhance the

ability to constrain the Z-axis during dynamic estimation. The multi-sensor distribution fusion incorporates total station lever arm error compensation and adaptive adjustments to LiDAR odometry weights. Compared to the single-engine method, LINS and RRR-MF, TBM-MSE excels in state estimation across different coal mine scenarios. After ablation and comparative experiments, the multi-engine estimation framework of TBM-MSE is validated as the optimal choice for TBM localization. TBM-MSE is capable of achieving globally consistent state estimation, even when operating in dusty and vibration-prone environments.

REFERENCES

- [1] L. Yake and L. Yueqiang, "Research on the automatic laser navigation system of the tunnel boring machine," in *Proc. 7th Int. Symp. Precis. Eng. Meas. Instrum.*, vol. 8321, 2011, pp. 484–489, doi: [10.1117/12.904848](https://doi.org/10.1117/12.904848).
- [2] Y. Du, M. Tong, T. Liu, and H. Dong, "Visual measurement system for roadheaders pose detection in mines," *Opt. Eng.*, vol. 55, no. 10, Oct. 2016, Art. no. 104107, doi: [10.1117/1.OE.55.10.104107](https://doi.org/10.1117/1.OE.55.10.104107).
- [3] S. Fu, Y. Li, K. Zong, C. Liu, D. Liu, and M. Wu, "Ultra-wideband pose detection method based on TDOA positioning model for boom-type roadheader," *AEU-Int. J. Electron. Commun.*, vol. 99, pp. 70–80, Feb. 2019, doi: [10.1016/j.aeu.2018.11.023](https://doi.org/10.1016/j.aeu.2018.11.023).
- [4] T. Shan, B. Englot, D. Meyers, W. Wang, C. Ratti, and D. Rus, "LIO-SAM: Tightly-coupled LiDAR inertial odometry via smoothing and mapping," in *Proc. IEEE/RSJ Int. Conf. Intell. Robots Syst. (IROS)*, Oct. 2020, pp. 5135–5142, doi: [10.1109/IROS45743.2020.9341176](https://doi.org/10.1109/IROS45743.2020.9341176).
- [5] T. Qin, P. Li, and S. Shen, "VINS-mono: A robust and versatile monocular visual-inertial state estimator," *IEEE Trans. Robot.*, vol. 34, no. 4, pp. 1004–1020, Aug. 2018, doi: [10.1109/TRO.2018.2853729](https://doi.org/10.1109/TRO.2018.2853729).
- [6] T. Shan, B. Englot, C. Ratti, and D. Rus, "LVI-SAM: Tightly-coupled LiDAR-visual-inertial odometry via smoothing and mapping," in *Proc. IEEE Int. Conf. Robot. Autom. (ICRA)*, May 2021, pp. 5692–5698, doi: [10.1109/ICRA48506.2021.9561996](https://doi.org/10.1109/ICRA48506.2021.9561996).
- [7] K. Ebadi, Y. Chang, M. Palieri, A. Stephens, A. Hatteland, E. Heiden, A. Thakur, N. Funabiki, B. Morrell, S. Wood, L. Carlone, and A.-A. Agha-Mohammadi, "LAMP: Large-scale autonomous mapping and positioning for exploration of perceptually-degraded subterranean environments," 2020, *arXiv:2003.01744*.
- [8] J. Zhang and S. Singh, "Low-drift and real-time LiDAR odometry and mapping," *Auto. Robots*, vol. 41, no. 2, pp. 401–416, Feb. 2017, doi: [10.1007/s10514-016-9548-2](https://doi.org/10.1007/s10514-016-9548-2).
- [9] C. Le Gentil, T. Vidal-Calleja, and S. Huang, "3D LiDAR-IMU calibration based on upsampled preintegrated measurements for motion distortion correction," in *Proc. IEEE Int. Conf. Robot. Autom. (ICRA)*, May 2018, pp. 2149–2155, doi: [10.1109/ICRA.2018.8460179](https://doi.org/10.1109/ICRA.2018.8460179).
- [10] W. Xu and F. Zhang, "FAST-LIO: A fast, robust LiDAR-inertial odometry package by tightly-coupled iterated Kalman filter," *IEEE Robot. Autom. Lett.*, vol. 6, no. 2, pp. 3317–3324, Apr. 2021, doi: [10.1109/LRA.2021.3064227](https://doi.org/10.1109/LRA.2021.3064227).
- [11] S. Chen, L. Nan, R. Xia, J. Zhao, and P. Wonka, "PLADE: A plane-based descriptor for point cloud registration with small overlap," *IEEE Trans. Geosci. Remote Sens.*, vol. 58, no. 4, pp. 2530–2540, Apr. 2020, doi: [10.1109/TGRS.2019.2952086](https://doi.org/10.1109/TGRS.2019.2952086).
- [12] T. Shan and B. Englot, "LeGO-LOAM: Lightweight and ground-optimized LiDAR odometry and mapping on variable terrain," in *Proc. IEEE Int. Conf. Intell. Robot. Syst.*, Oct. 2018, pp. 4758–4765, doi: [10.1109/IROS.2018.8594299](https://doi.org/10.1109/IROS.2018.8594299).
- [13] J. Graeter, A. Wilczynski, and M. Lauer, "LIMO: LiDAR-monocular visual odometry," in *Proc. IEEE/RSJ Int. Conf. Intell. Robots Syst. (IROS)*, Oct. 2018, pp. 7872–7879.
- [14] P. Geneva, K. Ekenhoff, Y. Yang, and G. Huang, "LIPS: LiDAR-inertial 3D plane SLAM," in *Proc. IEEE/RSJ Int. Conf. Intell. Robots Syst. (IROS)*, Oct. 2018, pp. 123–130, doi: [10.1109/IROS.2018.8594463](https://doi.org/10.1109/IROS.2018.8594463).
- [15] K. Li, M. Li, and U. D. Hanebeck, "Towards high-performance solid-state-LiDAR-inertial odometry and mapping," *IEEE Robot. Autom. Lett.*, vol. 6, no. 3, pp. 5167–5174, Jul. 2021, doi: [10.1109/LRA.2021.3070251](https://doi.org/10.1109/LRA.2021.3070251).
- [16] C. Qin, H. Ye, C. E. Pranata, J. Han, S. Zhang, and M. Liu, "LINS: A LiDAR-inertial state estimator for robust and efficient navigation," in *Proc. IEEE Int. Conf. Robot. Autom. (ICRA)*, May 2020, pp. 8899–8906, doi: [10.1109/ICRA40945.2020.9197567](https://doi.org/10.1109/ICRA40945.2020.9197567).
- [17] W. Xu, Y. Cai, D. He, J. Lin, and F. Zhang, "FAST-LIO2: Fast direct LiDAR-inertial odometry," *IEEE Trans. Robot.*, vol. 38, no. 4, pp. 2053–2073, Aug. 2022, doi: [10.1109/TRO.2022.3141876](https://doi.org/10.1109/TRO.2022.3141876).
- [18] C. Bai, T. Xiao, Y. Chen, H. Wang, F. Zhang, and X. Gao, "Faster-LIO: Lightweight tightly coupled LiDAR-inertial odometry using parallel sparse incremental voxels," *IEEE Robot. Autom. Lett.*, vol. 7, no. 2, pp. 4861–4868, Apr. 2022, doi: [10.1109/LRA.2022.3152830](https://doi.org/10.1109/LRA.2022.3152830).
- [19] G. Hu, S. Gao, and Y. Zhong, "A derivative UKF for tightly coupled INS/GPS integrated navigation," *ISA Trans.*, vol. 56, pp. 135–144, May 2015, doi: [10.1016/j.isatra.2014.10.006](https://doi.org/10.1016/j.isatra.2014.10.006).
- [20] G. Hu, B. Gao, Y. Zhong, L. Ni, and C. Gu, "Robust unscented Kalman filtering with measurement error detection for tightly coupled INS/GNSS integration in hypersonic vehicle navigation," *IEEE Access*, vol. 7, pp. 151409–151421, 2019, doi: [10.1109/ACCESS.2019.2948317](https://doi.org/10.1109/ACCESS.2019.2948317).
- [21] B. Gao, G. Hu, Y. Zhong, and X. Zhu, "Distributed state fusion using sparse-grid quadrature filter with application to INS/CNS/GNSS integration," *IEEE Sensors J.*, vol. 22, no. 4, pp. 3430–3441, Feb. 2022, doi: [10.1109/SEN.2021.3139641](https://doi.org/10.1109/SEN.2021.3139641).
- [22] S. Gao, Y. Zhong, X. Zhang, and B. Shirinzadeh, "Multi-sensor optimal data fusion for INS/GPS/SAR integrated navigation system," *Aerosp. Sci. Technol.*, vol. 13, nos. 4–5, pp. 232–237, Jun. 2009, doi: [10.1016/j.ast.2009.04.006](https://doi.org/10.1016/j.ast.2009.04.006).
- [23] B. Gao, G. Hu, S. Gao, Y. Zhong, and C. Gu, "Multi-sensor optimal data fusion for INS/GNSS/CNS integration based on unscented Kalman filter," *Int. J. Control. Autom. Syst.*, vol. 16, no. 1, pp. 129–140, Feb. 2018, doi: [10.1007/s12555-016-0801-4](https://doi.org/10.1007/s12555-016-0801-4).
- [24] S. Zhao, H. Zhang, P. Wang, L. Nogueira, and S. Scherer, "Super odometry: IMU-centric LiDAR-visual-inertial estimator for challenging environments," in *Proc. IEEE/RSJ Int. Conf. Intell. Robots Syst. (IROS)*, Sep. 2021, pp. 8729–8736, doi: [10.1109/IROS51168.2021.9635862](https://doi.org/10.1109/IROS51168.2021.9635862).
- [25] Y. Liu, H. Wang, Z. Wu, and R. Hu, "RRR-MF: Time-domain feature reconstruction of road roughness in front of anchor machine via multi-modal fusion," *Measurement*, vol. 199, Aug. 2022, Art. no. 111408, doi: [10.1016/j.measurement.2022.111408](https://doi.org/10.1016/j.measurement.2022.111408).
- [26] A. Reinke, M. Palieri, B. Morrell, Y. Chang, K. Ebadi, L. Carlone, and A. Agha-Mohammadi, "LOCUS 2.0: Robust and computationally efficient LiDAR odometry for real-time 3D mapping," *IEEE Robot. Autom. Lett.*, vol. 7, no. 4, pp. 9043–9050, Oct. 2022. [Online]. Available: <https://hdl.handle.net/1721.1/145303>
- [27] M. Xiao, W. Zhang, Y. Zhao, X. Xu, and S. Zhou, "Fault diagnosis of gearbox based on wavelet packet transform and CLSPSO-BP," *Multimedia Tools Appl.*, vol. 81, no. 8, pp. 11519–11535, Mar. 2022, doi: [10.1007/s11042-022-12465-3](https://doi.org/10.1007/s11042-022-12465-3).
- [28] B. Shi, Y. Su, D. Zhang, C. Wang, and M. S. AbouOmar, "Research on trajectory reconstruction method using automatic identification system data for unmanned surface vessel," *IEEE Access*, vol. 7, pp. 170374–170384, 2019, doi: [10.1109/ACCESS.2019.2955440](https://doi.org/10.1109/ACCESS.2019.2955440).
- [29] M. Huang, Y. Liu, G. Yang, and X. Zhou, "An innovation based DFA and EMD method for denoising fiber optic gyroscope drift signal," in *Proc. 3rd Int. Conf. Inf. Sci. Control Eng. (ICISCE)*, Jul. 2016, pp. 1262–1266, doi: [10.1109/ICISCE.2016.270](https://doi.org/10.1109/ICISCE.2016.270).
- [30] L. Qian, G. Xu, W. Tian, and J. Wang, "A novel hybrid EMD-based drift denoising method for a dynamically tuned gyroscope (DTG)," *Measurement*, vol. 42, no. 6, pp. 927–932, Jul. 2009, doi: [10.1016/j.measurement.2009.01.017](https://doi.org/10.1016/j.measurement.2009.01.017).
- [31] G. Yang, Y. Liu, Y. Wang, and Z. Zhu, "EMD interval thresholding denoising based on similarity measure to select relevant modes," *Signal Process.*, vol. 109, pp. 95–109, Apr. 2015, doi: [10.1016/j.sigpro.2014.10.038](https://doi.org/10.1016/j.sigpro.2014.10.038).
- [32] N. El-Sheimy, H. Hou, and X. Niu, "Analysis and modeling of inertial sensors using Allan variance," *IEEE Trans. Instrum. Meas.*, vol. 57, no. 1, pp. 140–149, Jan. 2008, doi: [10.1109/TIM.2007.908635](https://doi.org/10.1109/TIM.2007.908635).
- [33] J. E. Bortz, "A new mathematical formulation for strapdown inertial navigation," *IEEE Trans. Aerosp. Electron. Syst.*, vol. AES-7, no. 1, pp. 61–66, Jan. 1971, doi: [10.1109/TAES.1971.310252](https://doi.org/10.1109/TAES.1971.310252).
- [34] R. Valenti, I. Dryanovski, and J. Xiao, "Keeping a good attitude: A quaternion-based orientation filter for IMUs and MARGs," *Sensors*, vol. 15, no. 8, pp. 19302–19330, Aug. 2015, doi: [10.3390/s150819302](https://doi.org/10.3390/s150819302).

- [35] C. Hertzberg, R. Wagner, U. Frese, and L. Schröder, "Integrating generic sensor fusion algorithms with sound state representations through encapsulation of manifolds," *Inf. Fusion*, vol. 14, no. 1, pp. 57–77, Jan. 2013, doi: [10.1016/j.inffus.2011.08.003](https://doi.org/10.1016/j.inffus.2011.08.003).
- [36] S. Zhao, Z. Fang, H. Li, and S. Scherer, "A robust laser-inertial odometry and mapping method for large-scale highway environments," in *Proc. IEEE/RSJ Int. Conf. Intell. Robots Syst. (IROS)*, Nov. 2019, pp. 1285–1292, doi: [10.1109/IROS40897.2019.8967880](https://doi.org/10.1109/IROS40897.2019.8967880).



HONGWEI WANG received the Ph.D. degree in safety technology and engineering from Liaoning Technical University, Fuxin, China, in 2016. She is currently a Professor and the Director of the Shanxi Engineering Research Center for Coal Mine Intelligent Equipment. Her research interest includes coal mine intelligent equipment.



YU LIU received the M.S. degree in control engineering from the Taiyuan University of Technology, Taiyuan, China, in 2020, where he is currently pursuing the Ph.D. degree in mechanical and electrical engineering. His current research interests include LiDAR SLAM, inertial navigation, and deep learning.



LEI TAO received the B.S. degree in mechanical engineering from the Taiyuan University of Science and Technology, Taiyuan, China, in 2010. He is currently a Professor with the Shanxi Engineering Research Center for Coal Mine Intelligent Equipment. His research interests include coal mine intelligent equipment and coal mine special robots.

...